Coarsening phenomena of metal nanoparticles and the influence of the support pre-treatment: Pt/TiO₂(110)

F. Behafarid, B. Roldan Cuenya *

Department of Physics, University of Central Florida, Orlando, FL 32816, United States

ABSTRACT

One of the technologically most important requirements for the application of oxide-supported metal nanoparticles (NPs) in the fields of molecular electronics, plasmonics, and catalysis is the achievement of thermally stable systems. For this purpose, a thorough understanding of the different pathways underlying thermally-driven coarsening phenomena, and the effect of the nanoparticle synthesis method, support morphology, and degree of support reduction on NP sintering is needed. In this study, the sintering of supported metal NPs has been monitored via scanning tunneling microscopy combined with simulations following the Ostwald ripening and diffusion-coalescence models. Modifications were introduced to the diffusion-coalescence model to incorporate the correct temperature dependence and energetics. Such methods were applied to describe coarsening phenomena of physical-vapor deposited (PVD) and micellar Pt NPs supported on TiO₂(110). The TiO₂(110) substrates were exposed to different pre-treatments, leading to reduced, oxidized and polymer-modified TiO₂ surfaces. Such pre-treatments were found to affect the coarsening behavior of the NPs.

No coarsening was observed for the micellar Pt NPs, maintaining their as-prepared size of ~3 nm after annealing in UHV at 1060 °C. Regardless of the initial substrate pre-treatment, the average size of the PVD-grown NPs was found to increase after identical thermal cycles, namely, from 0.5 ± 0.2 nm to 1.0 ± 0.3 nm for pristine TiO₂, and from 0.8 ± 0.3 nm to 1.3 ± 0.6 nm for polymer-coated TiO₂ after identical thermal treatments. Although no direct real-time in situ microscopic evidence is available to determine the dominant coarsening mechanism of the PVD NPs unequivocally, our simulations following the diffusion-coalescence coarsening route were in significantly better agreement with the experimental data as compared to those based on the Ostwald-ripening model. The enhanced thermal stability of the micellar NPs as compared to the PVD clusters might be related to their initial larger NP size, narrower size distribution, and larger interparticle distances.

1. Introduction

The unusual structural, electronic, magnetic, and chemical properties of metal nanoparticles (NPs) have found numerous applications in technologically important areas such as catalysis, molecular electronics, and plasmonics [1–4]. Nevertheless, in order to take advantage of these new material systems in a real-world industrial setting, a thorough understanding is needed of how those properties evolve under environmental conditions such as elevated temperatures and exposure to liquid/gas reactants. Although new developments in NP synthesis methods provide the capability of fabricating NPs in the sub-nanometer size regime, unwanted coarsening phenomena commonly lead to the disappearance of the small NP sizes and a broadening of initially narrow size distributions. This is a major drawback in fields such as catalysis, because a number of chemical processes are structure sensitive, and thermally-induced changes in NP size and shape can result in a dramatic drop of activity due

to the loss of surface area [5], a change in selectivity toward unwanted byproducts, as well as catalyst deactivation [6].

The present study provides insight into an important aspect influencing the commercial use of oxide-supported metal NPs, namely, their tendency to coarsen at elevated temperatures. Despite the fact that in industrially relevant catalytic combustion processes NP sintering occurs at elevated temperatures (~900 °C) [7–11], most of the basic in situ studies published to date describe a much lower temperature regime. We study here coarsening phenomena in physical vapor deposited (PVD) and micellar Pt NPs at more realistic temperatures, namely, in the temperature regime of 930 °C to 1060 °C. We also pay attention to the effect of the substrate pretreatment (morphology and state of reduction) on the NP coarsening mechanisms. Our model system, Pt/TiO₂, is presently extensively used in catalysis applications such as water splitting [12], sulfuric acid decomposition [10], and photo-oxidation reactions [13].

Coarsening phenomena in nanoscale systems have been the subject of intensive research efforts since a number of years, with particular emphasis given to the effect of the initial NP size and size distribution [14–17], as well as structure, morphology, and stoichiometry of the

* Corresponding author. Tel.: +1 4078231883; fax: +1 4078235112.
E-mail address: roldan@ucf.edu (B. Roldan Cuenya).

support [17–21]. Two main coarsening pathways have been considered: (i) Ostwald ripening, in which individual atoms detach from small clusters and diffuse over the support surface until they join larger NPs, and (ii) diffusion coalescence, in which entire NPs diffuse across the support surface until they coalesce with other NPs. Previous literature reports have described coarsening phenomena in metal NP systems based on either model or a combination of both, a distinction which was proven to be strongly dependent on the specific material system under investigation. For instance, Thiel et al. [17] reported different coarsening trends for Ag islands on a Ag single crystal depending on the orientation of the substrate surface, with Ostwald-ripening phenomena preferentially occurring on Ag(111), and diffusion-coalescence on Ag(100). Additionally, the dominant coarsening pathway was also found to be susceptible to changes in the annealing temperature, time, and chemical environment, with oxidizing environments typically leading to Ostwald ripening, and reducing atmospheres to diffusion-coalescence [22]. Furthermore, a transition from diffusion-coalescence to Ostwald-ripening was described for Cu islands on Cu(100) with increasing temperature from 300 K to 343 K. On more closely related systems to the one under study here, Ostwald ripening phenomena were held responsible for the sintering of Au NPs on TiO$_2$ [16,23], while diffusion-coalescence processes were found to occur for Pd on TiO$_2$ [19,20,24].

Numerous previous studies have used the evolution of the NP size or the shape of the NP size histogram as an indirect diagnostic tool to get insight into the underlying coarsening mechanism, namely, whether it is Ostwald ripening or diffusion/coalescence [16,19,20,22,25–31]. Following conventional coarsening models [25–30], NP size distributions with a tail skewed toward lower NP sizes and a sharp cut-off have been commonly assigned to Ostwald ripening processes, while distributions with a long tail (log-normal distribution) toward large NP sizes have been attributed to processes dominated by NP diffusion and coalescence. Surprisingly, the majority of experimental NP size distributions available in the literature are of the log-normal type [30,32], even for processes where Ostwald-ripening has been demonstrated to be the main coarsening mechanism [22,31]. In the past, such discrepancy was attributed to the limitations of most microscopic methods at detecting small NPs, but this is not true for the most recent studies [22,32]. The work by Datye et al. [22] demonstrates that the shape of the NP size distribution cannot be used to discern different coarsening mechanisms, especially in cases where Ostwald ripening and diffusion coalescence processes may occur simultaneously. In such complex cases, the small NPs that should be always present during Ostwald ripening processes could quickly disappear due to their enhanced size-dependent mobility if the diffusion/coalescence pathway occurs concurrently. Furthermore, in cases where the initial NP size distribution might be of the log-normal type, it might take a very long time for a low-size tail to develop in the size histogram, even when Ostwald ripening is dominant.

A better agreement between experimental data and coarsening simulations following the Ostwald ripening model was obtained by Parker and Campbell [14–16] by incorporating a size-dependent surface energy in their model and by using an exponential function in the formulation of the ripening rates instead of a first-order approximation of the associated Taylor series. Both modifications lead to less asymmetric NP size histograms, although broadening and a low-size tail were still observed. Using the mean field approximation, a model for diffusion-coalescence processes was introduced by Smoluchowski [25,26]. Assuming a simple power law for the NP's diffusion coefficient, the scaling behavior of this model was studied by Kandel [29], and a size histogram with a tail skewed toward larger sizes was found to gradually develop over long periods of time [29]. However, the former model fails at providing the correct description of coarsening phenomena occurring over short periods of time.

Despite the high level of detail included in the various coarsening models available [16,20,29], relatively little attention has been given

to the effect of the morphology and stoichiometry of the NP support, the strength of the NP/support bonding, and the NP synthesis method. In the present work we use a combination of controlled NP preparation, STM, and theoretical modeling to address these effects. First, we use bench-mark Pt NPs grown by PVD in ultrahigh vacuum (UHV) on pristine TiO$_2$(110) surfaces to illustrate NP mobility, step decoration and coarsening phenomena. Secondly, we introduce modifications in the morphology and reducibility of the TiO$_2$ support (polymer-coating followed by an oxygen plasma treatment) to mimic the preparation conditions of micellar NPs, and study how such modifications relate to the observed changes in the coarsening behavior. Finally, we discuss the enhanced thermal stability of the self-assembled and geometrically well-defined metal NPs synthesized by inverse micelle encapsulation methods [33,34]. The narrow NP size distributions that can achieved by using the latter synthesis allow us to better follow any coarsening phenomena occurring in these samples, since log-normal distributions with tails skewed toward high NP sizes are not present on the as-prepared samples.

2. Experimental and theoretical methods

2.1. Sample preparation

Two samples were synthesized by evaporating submonolayer coverages (0.09 ML) of Pt on two differently-prepared TiO$_2$(110) substrates at a deposition rate of 1.5×10^{-3} ML/s (1 ML is defined as 1.5×10^{15} atoms/cm^2) measured by a quartz microbalance. Sample 1 (S1) consisted of Pt NPs evaporated at room temperature on pristine TiO$_2$(110) and subsequently annealed in UHV at 830 °C, 930 °C, 1030 °C and 1060 °C for 10 min. Prior to the deposition of Pt the TiO$_2$(110) crystal was cleaned by several cycles of Ar$^+$ sputtering (P[Ar$^+$] = 1×10^{-6} mbar, 1 keV, 5 µA) for 45 min and annealing at 900–1000 °C for 20 min. This procedure was repeated until large (1×2)-TiO$_2$ terraces were observed by STM [35]. All experiments were conducted on a TiO$_2$(110) crystal of dark blue color, which indicates its bulk reduction. Such crystal has sufficient conductivity for STM imaging, and displays a bandgap of about 3.2 eV according to our scanning tunneling spectroscopy measurements (Suppl. Fig. S1).

In order to test whether the roughness of the substrate (*e.g.* terrace width, presence of defects, etc.) and/or stoichiometry (degree of TiO$_2$ reduction) affects the coarsening behavior of the deposited NPs, a second sample (S2) with a polymer-modified [PS(27700)-P2VP(4300) dissolved in toluene] surface was prepared. The same Pt coverage as in S1 (0.09 ML) was evaporated at room temperature on the polymer-modified TiO$_2$(110) support (S2).

A third sample consisted of micellar Pt NPs supported on TiO$_2$(110) (S3) prepared by reverse micelle encapsulation [33] as described in detail elsewhere [2,34,36–38]. The diblock copolymer used for this synthesis was the same one employed to modify the TiO$_2$ surface in S2, with the difference that in the latter case the polymeric micelles were loaded with Pt, with a metal salt-to-P2VP weight ratio of 0.6.

Sample 1 was prepared in UHV, while S2 and S3 were introduced into our UHV system after substrate functionalization with the PS-P2VP polymer (before Pt NP deposition for S2 and after the dip-coating of the micellar Pt NPs for S3). The removal of the polymer ligands from S3 was achieved by an *in situ* O$_2$-plasma treatment (O$_2$ pressure = 4×10^{-5} mbar, 120 min) at room temperature. Sample 2 was subjected to an analogous treatment to remove the polymer from the substrate surface after the deposition of Pt in UHV. X-ray photoelectron spectroscopy (XPS) measurements (Al–K$_\alpha$, 1486.6 eV) conducted after the latter treatment corroborated the complete disappearance of the polymeric C-1s signal from the micellar sample (S3). Although the C-1s signal completely disappeared after the O$_2$-plasma for S3 (micellar NPs surrounded by a thin polymeric layer), a small C signal was detected for S2 (evaporated NPs deposited on a thick polymer layer) after the first annealing treatment at 930 °C, which was assigned to

polymeric carbon leftover from the TiO$_2$ pre-treatment likely trapped underneath the NPs. Nevertheless, no C was detected by XPS for any of the samples after the subsequent annealing at high temperature (>930 °C) (see Suppl. Fig. S2), which is the starting point of our coarsening study. After the atomic oxygen exposure, the micellar sample (S3) was isochronally annealed in UHV in 100 °C intervals from 300 °C to 900 °C for 20 min and from 1000 °C to 1060 °C for 10 min. Sample 2 experienced a thermal treatment identical to that of S1. The NPs in S2 and S3 are oxidized (PtO$_2$) after the O$_2$-plasma treatment but subsequently reduced after annealing above 300 °C [39].

The comparison of all three samples directly after NP deposition at RT was not possible due to the strong enhancement of the roughness of the TiO$_2$ substrate observed after the O$_2$-plasma treatment applied to S2 and S3 to remove the organic ligands used in the synthesis. Such treatment gives rise to TiO$_x$ clusters on the support surface which cannot be easily distinguished from small Pt NPs based exclusively on morphological measurements. Therefore, the comparison of the sintering behavior of all three samples was done after an annealing treatment above 900 °C, which was found to lead to a flatter TiO$_2$ morphology that could be atomically resolved.

STM images were acquired at room temperature after annealing from 930 °C to 1060 °C. An electrochemically-etched W tip was used. The tip was cleaned in UHV by Ar$^+$ sputtering before each STM session. The base pressure of the STM chamber was 1×10^{-10} mbar. The scanning parameters used were: $I_t = 0.1$ nA and $V_t = 1.2$ V. Due to tip convolution effects, the NP diameter obtained by STM overestimates the real diameter [19,20,40,41], and since the tip shape might also change during the measurements, it cannot be reliably used for comparison purposes. Since the measured NP height is independent of the tip shape, it is used here as representative size parameter. Throughout this manuscript, when NPs were observed at TiO$_2$ step-edges, the average height of the top and bottom TiO$_2$ terraces was used as height reference.

2.2. Simulation methods

The following models have been applied to simulate the coarsening mechanisms of Pt NPs prepared using two distinct synthesis methods (PVD and micelle encapsulation) and supported on differently treated TiO$_2$(110) surfaces. Each simulation requires two sets of measurements: (i) one initial experimental NP size distribution as the starting point of the simulation which is being subjected to a thermal treatment, and (ii) a measurement of the final state of the sample (size histogram) after the thermal treatment, which is used to compare with the results of the simulation. Therefore, based on three sets of STM images acquired after annealing at 930 °C, 1030 °C and 1060 °C, two sets of simulations can be carried out: (i) from 930 °C to 1030 °C, and (ii) from 1030° to 1060 °C. The former will be compared with the experimental 1030 °C and 1060 °C STM size histograms, respectively.

2.2.1. Ostwald ripening

Following the Ostwald-ripening model, atoms detach from small NPs and move randomly over the substrate surface until they find another particle to join. It should be considered that small NPs lose atoms at a higher rate as compared to larger clusters due to size-dependent energetics. As a result of this phenomenon, the larger particles grow in size at the expense of the smaller ones, until the latter completely disappear. The overall result is a shift of the NP size distribution to higher values and a decrease in the density of NPs on the substrate surface. For an interface-limited Ostwald-ripening process, in which the rate limiting step is the detachment of metal atoms from the NP perimeter (in contact with the support), the rate of change of the size of a particle with radius R is [14,16,27,28]:

$$\frac{dR}{dt} = \frac{K}{R} \exp\left[\frac{-E_{tot}}{k_B T}\right] \left(\exp\left[\frac{E(R^*)}{k_B T}\right] - \exp\left[\frac{E(R)}{k_B T}\right] \right), \tag{1}$$

where k_B is the Boltzmann constant and R^* is a critical NP radius that represents a NP size in unstable equilibrium for which the particle radius remains constant due to a compensation effect based on the number of incoming atoms arriving to a NP being the same as that of the atoms leaving the particle. $E(R)$ is the difference between the heat of adsorption of a metal atom in a NP of radius R and the corresponding bulk sublimation enthalpy (H_{sub} in Suppl. Fig. S3), E_{tot} is the total energy barrier of the system, and K is a parameter which depends on the specific NP material, the vibrational frequency of a monomer on the NP, and the contact angle of the metal NP with the support (assumed to be 90° here) [15,16,27,28].

Since the surface energy is expected to be size-dependent for NPs smaller than ~5 nm, the formulation of the heat of sublimation previously used by other groups [18–20,27,30] assuming a constant surface energy and giving rise to a $1/R$ size dependency is not valid for the calculations of $E(R)$ in Eq. (1). Instead, the modified bond-additivity model (MBA) must be used [14–16]. Suppl. Fig. S3 displays the heats of sublimation that we have extracted following the MBA model using Wulff-like NP shapes [1,42–44] instead of previously considered pyramidal shapes [14–16]. The former shapes are expected to be a better representation of the most commonly observed experimental NP geometries [1,42–44]. $E(R)$ was obtained by subtracting the heat of sublimation of bulk Pt (563 kJ/mol) from that obtained from the MBA model for the Pt NPs (Suppl. Fig. S3).

In addition, the critical radius (R^*) in Eq. (1) should be defined in a way that satisfies the mass conservation pre-requisite, e.g., no atoms are expected to be lost during the coarsening process at the particular temperatures considered [45]. We have ensured mass conservation by setting $\Sigma\, dV_{tot}/dt = 0$, where V_{tot} is the total volume of the NPs. This allows us to determine the critical energy $E(R^*)$ in Eq. (1) following:

$$E(R^*) = k_B T \ln\left[\sum R_i \exp\left[\frac{E(R_i)}{k_B T}\right] / \sum R_i \right]. \tag{2}$$

One important practical challenge in the use of Eq. (1) to obtain the time dependent $R(t)$ for many particles is the fact that widely different time scales are involved in the coarsening. The reduction of the size of NPs with a radius well below the critical radius and the continued reappearance of small clusters occur extremely rapidly at elevated temperatures (10^{-4}–10^{-7} s). In order to follow such effects while maintaining mass conservation using Eq. (2), very fine time steps are needed in the models during the entire thermal treatment [45]. Such small time steps result in computationally intensive calculations, especially for the industrially relevant time scales of coarsening, which are in the order of months to years. To overcome this issue we have introduced a new method to reduce the computation time by several orders of magnitude while ensuring mass conservation. Our approach is to use numerical methods to find the effective critical energy $E(R^*)$ that conserves the total mass during the desired time step (as large as several seconds). The change in the total volume (ΔV) obtained from an initial guess of R^* is calculated, and a bisection method implemented to find the root of $\Delta V[E(R^*)]$. Since the change in R^* is gradual, the bisection method was found to converge very fast, and $E(R^*)$ can be calculated within a few iterations. Therefore, instead of running the simulation with a very fine time step (e.g. a time step of 10^{-5} s needs 10^5 calculations for each second of simulation), similar results satisfying mass conservation can be achieved by using larger time steps (e.g. 1 s) and doing just a few numerical calculations.

2.2.2. Diffusion-coalescence

In addition to the model discussed above, the possibility of particle diffusion and sintering must also be taken into account. Following the

mean field approximation, the rate of change of the density of NPs on a substrate is given by [18–20,25,26]:

$$\frac{\partial f(v,t)}{\partial t} = \int_0^v D_c(v')f(v',t)f(v-v',t)dv' - \int_0^\infty \left[D_c(v) + D_c(v')\right]f(v,t)f(v',t)dv',$$

(3)

where D_c is the diffusion constant of the NPs [18–20], v is the NP volume, and $f(v)$ is the density of NPs with volume v. It is assumed that the NPs are distributed randomly on the support and that the probability of interparticle collision is proportional to their surface density as well as to their mobility.

The diffusion constant of the NPs (D_c) is proportional to the density of adatoms on the NP surface (ρ) and has a $1/r^4$ size dependence [18–20]. However, the previous formulations were only valid for the comparison of isothermal experiments [18,19]. In order to overcome this shortcoming, we have introduced the following expression for ρ:

$$\rho = \rho_0 \exp\left[\frac{-E_{AF}(R)}{k_B T}\right],$$

(4)

where ρ_0 is the density of adatoms at infinite T, which is the same as the surface density of metal atoms [$\approx 1.5 \times 10^{19}$ atoms/m^2 for the platinum (111) surface]. The adatom formation energy barrier (E_{AF}) is the energy needed for an atom to migrate from the core of the NP to the surface, and is equal to the heat of sublimation minus the binding energy of the adatom to the surface. Here, the size effect is implicitly included in $E_{AF}(R)$, and therefore, using the proper $E_{AF}(R)$ is the key to obtain the correct diffusion equation. We have used in our simulations the results of molecular dynamics (MD) and nudged elastic band (NEB) calculations by Yang et al. [46] for the adatom formation energy of clusters with Wulff polyhedral shape, Suppl. Fig. S3.

Following the above considerations, a modified description of the diffusion coefficient of a NP with radius R is proposed:

$$D_c(R,T) = K_S \rho_0 D_0^{Pt} \frac{3\Omega^2}{\pi R^4} \exp\left[\frac{-(E_d + E_{AF})}{k_B T}\right],$$

(5)

where K_S is a constant which takes into account the support effect, D_0^{Pt} is a pre-exponential factor of Pt, E_d is the Pt self-diffusion barrier. Ω is the Pt atomic volume, and R is the NP radius.

Eqs. (3) and (5) can be used to calculate the time evolution of the NP size distribution. We have introduced an efficient matrix-based calculation to simulate Eq. (3), which is equivalent to its direct integration, but that overcomes the statistical errors associated with the random collision method [29]. First, a volume vector $\mathbf{V}$ is constructed containing monotonically increasing values of NP volumes, v_i. Then, for a given instant of time, the volume histogram vector is constructed, $\mathbf{F}_i = f(v_i)$, in which each element contains the population of NPs with volume v_i. In the next step, the diffusion coefficient vector $\mathbf{D}_i = \mathbf{D}(v_i)$ is calculated, with each element being the diffusion coefficient of a cluster with size v_i. The time evolution matrix is given by:

$$\mathbf{T} = \mathbf{F}^T(\mathbf{D} \circ \mathbf{F}) \text{ or } \mathbf{T}_{ij} = \mathbf{F}_i\left(\mathbf{D}_j.\mathbf{F}_j\right),$$

(6)

where "o" denotes the Hadamard product of the two matrixes. $\mathbf{T}_{ij}$ is the collision rate of clusters with volume v_j moving toward clusters with volume v_i. This simple matrix multiplication provides all the information needed to determine the time evolution of a NP size distribution within a given time step. The change in the population of clusters with volume v_i after a time step dt is obtained from:

$$df(v_i) = \sum_{k=j-i} \mathbf{T}_{jk}dt - \sum_j \left(\mathbf{T}_{ij} + \mathbf{T}_{ji}\right)dt,$$

(7)

where the first and second terms on the right hand side, represent the first and second integrals in Eq. (3).

3. Results

3.1. Pt NPs evaporated on pristine TiO$_2$(110)

Fig. 1 displays room temperature STM images of NPs grown by evaporating 0.09 ML of Pt on pristine (sputtered/annealed) TiO$_2$(110). The images correspond to a sample that was subsequently isochronally annealed in UHV at 930 °C (a,b), 1030 °C (c,d), and 1060 °C (e,f) for 10 min (S1). The atomically-resolved (1×2) reconstruction of the partially reduced TiO$_2$(110) support can be seen in these images. This surface reconstruction is typical of strongly reduced TiO$_2$ surfaces [18,35]. Fig. 1 shows the presence of Pt NPs over the entire TiO$_2$ surface at 930 °C. However, with increasing annealing temperature (>1000 °C), preferential decoration of TiO$_2$ step sites is observed, although some NPs still remain on terraces of the support even at 1060 °C. The steps on this TiO$_2$ surface are not primarily oriented along [001], which is known to be one of the most stable step orientations after high temperature annealing [18]. The latter is assigned to insufficient annealing time during our experiments to achieve the most stable step orientation.

Histograms of the NP height and interparticle distance obtained from these STM images are included in Fig. 2. An increase in the average NP height from 0.5 ± 0.2 nm to 1.0 ± 0.3 nm is observed with increasing annealing temperature from 930 °C to 1060 °C, Fig. 2(a). As expected in
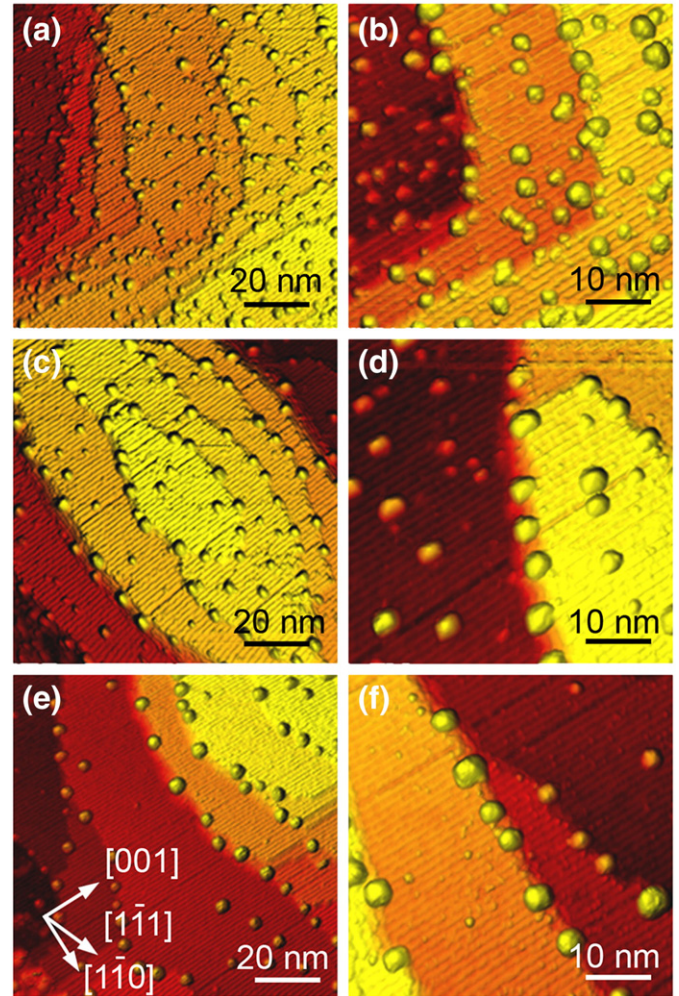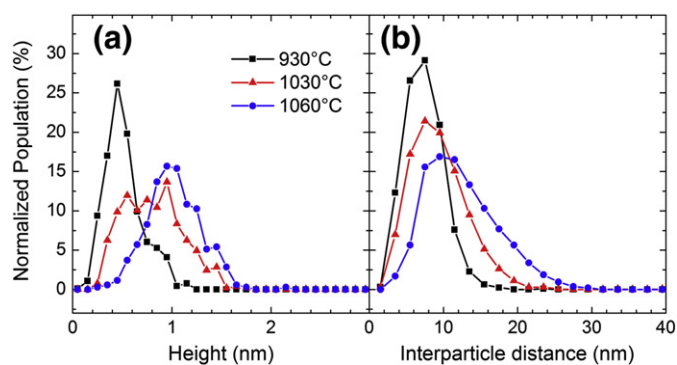

Fig. 1. STM images of 0.09 ML of Pt evaporated on pristine TiO$_2$(110) acquired at room temperature after annealing in UHV at 930 °C (a,b), 1030 °C (c,d), and 1060 °C (e,f) for 10 min.

Fig. 2. Height (a) and interparticle distance (b) histograms obtained from the STM data of Pt NPs evaporated on pristine TiO$_2$(110) shown in Fig. 1 after annealing at 930 °C (squares), 1030 °C (triangles), and 1060 °C (circles).

coarsening processes, the increase in the NP height is accompanied by a parallel decrease in the NP density on the support, Table 1(a), and an increase in the interparticle distance, Fig. 2(b).

As mentioned before, the NP diameter obtained via STM for 3D NPs cannot be trusted due to tip-convolution effects [18–20,40,41]. However, STM measurements provide reliable information on the NP height (h) and surface density, parameters that in combination with the total evaporated thickness estimated from the quartz microbalance can be used to gain insight into the NP shape. By assuming that no material has been lost during the different annealing treatments, the total volume of all Pt NPs in our sample should be the same at each temperature. This volume can be extracted from the quartz microbalance measurements. In order to gain insight into the NP shape (aspect ratio φ = height/radius), an initial guess of the shape can be made, for example, hemispherical, and the total volume of Pt can be calculated based on the STM-measured NP height and cluster density. If the latter total STM volume is different from the one obtained from the quartz microbalance, it could be concluded that a wrong assumption for the NP shape was made, and that a different aspect ratio must be considered. Following this idea, the NP aspect ratio can be adjusted ($0<\varphi<2$) for all STM measurements at a given temperature in order to satisfy the mass conservation criterion. For truncated spherical NPs (of radius R and height <2R), the NP volume is obtained from: $v_i = (1/\varphi - 1/3)\pi h_i^3$. These calculations were done using individual NP heights (h_i) measured by STM. Table 1 shows the calculated aspect ratios following the above approach after each annealing treatment. The aspect ratios correspond to an average of those from small and large NPs present on the support surface at a given temperature. An increase in the average aspect ratio is observed with increasing average

NP size (height), suggesting that NP-support interactions are weaker for the larger NPs. Although this result is obtained for truncated spherical NP shapes, it is also expected to be valid for other shapes.

Since the pristine substrate was already annealed at high temperature before Pt evaporation, the support is not expected to change significantly upon annealing [the original (1×2) reconstruction remains], and the change in the shape of the NPs cannot be attributed to morphological changes of the support surface. For our 3D NPs, the larger the NPs, the lower will be the influence of interfacial effects. A similar effect was reported by Yang et al. [47], since Au NPs larger than 4.6 Å deposited on TiO$_2$(110) were found to be less sensitive to the oxygen content on the TiO$_2$ surface than smaller NPs. Jak et al. [18–20] also described an increase in the aspect ratio of Pd NPs supported on TiO$_2$(110) upon annealing treatments in UHV at 672 K.

3.2. Pt NPs evaporated on polymer-modified TiO$_2$(110)

In order to test whether the roughness of the substrate (*e.g.* terrace width, presence of defects, etc.) and/or stoichiometry (degree of TiO$_2$ reduction) can affect the mobility of the deposited NPs, we have prepared a second sample in which the clean pristine TiO$_2$(110) substrate was initially *ex situ* coated by a thin layer of the PS-P2VP diblock copolymer. Pt NPs (0.09 ML) were evaporated in UHV on the polymer-coated TiO$_2$ surface at room temperature and subsequently exposed to an O$_2$-plasma treatment and isochronal annealing from 930 °C to 1060 °C for 10 min, Fig. 3. Although the strong reduction of our bulk TiO$_2$(110) crystal used

Table 1
Average NP height (h), interparticle distance (IP), density of NPs on the support, and aspect ratio extracted from the analysis of RT STM images acquired after annealing at the indicated temperatures. The data displayed correspond to Pt NPs evaporated on (a) pristine TiO$_2$(110), (b) polymer-coated TiO$_2$(110), and (c) micellar Pt NPs deposited on TiO$_2$(110). The standard deviations are included in parenthesis.
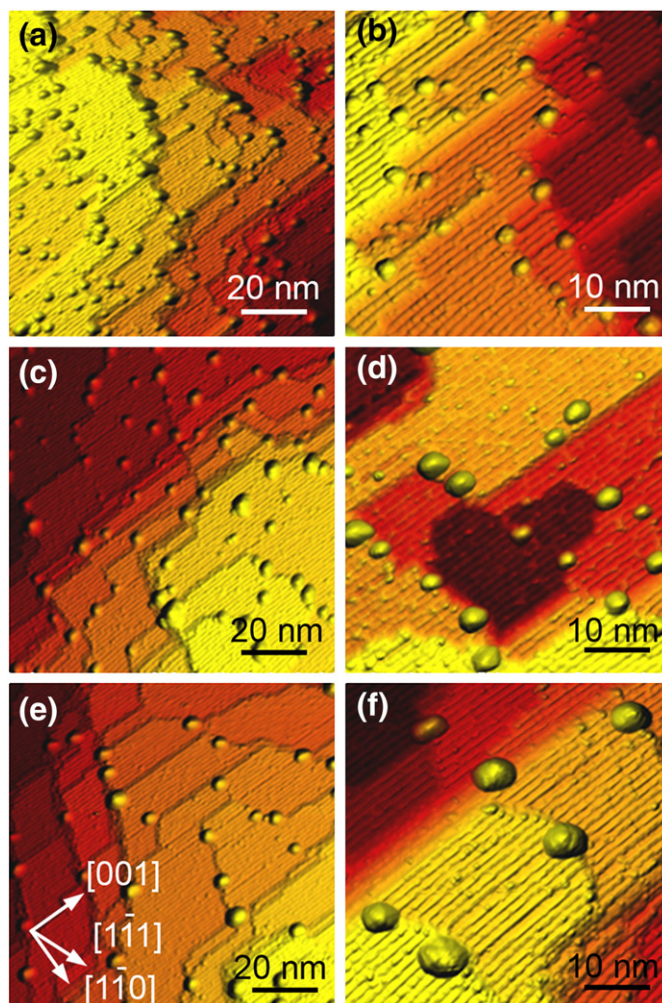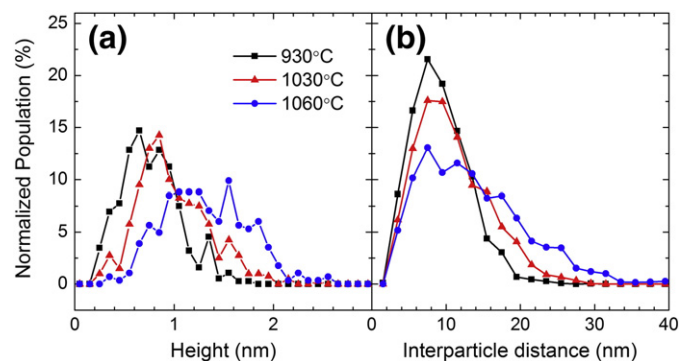
	Height (nm)	IP distance (nm)	Surface density (NP/m$^2 \times 10^{15}$)	Aspect ratio φ
(a) Pt NPs evaporated on pristine TiO$_2$(110) — S1				
930 °C	0.5 (2)	7 (3)	25.6	0.6
1030 °C	0.8 (3)	9 (4)	11.3	0.9
1060 °C	1.0 (3)	12 (5)	7.3	1.0
(b) Pt NPs evaporated polymer-coated TiO$_2$(110) — S2				
930 °C	0.8 (3)	9 (4)	13.5	0.9
1030 °C	1.0 (4)	11 (5)	7.5	1.0
1060 °C	1.3 (6)	13 (7)	3.8	1.1
(c) Micellar Pt NPs deposited on pristine TiO$_2$(110) — S3				
1000 °C	3.1 (6)	28 (5)	1.3	–
1060 °C	3.0 (7)	31 (7)	1.3	–
1060 °C 2nd	3.0 (9)	30 (7)	1.4	–

Fig. 3. STM images of 0.09 ML of Pt evaporated on polymer-coated TiO$_2$(110) taken at room temperature after an O$_2$-plasma treatment and subsequent annealing at 930 °C (a,b), 1030 °C (c,d), and 1060 °C (e,f) for 10 min.

in these experiments was evident from its dark blue color, the former treatment results in a lower degree of reduction of the TiO$_2$ surface as compared to the pristine sample. Nevertheless, after our high temperature annealing, the same (1×2) reconstruction is observed for both samples. The STM images in Fig. 3 reveal a rougher morphology (narrow terraces) of the TiO$_2$ surface after the above treatment as compared to pristine TiO$_2$, which is characterized by much wider terraces at the same temperatures. Moreover, straight TiO$_2$ steps with a preferential [001] orientation are observed in the polymer-coated TiO$_2$ sample after O$_2$-plasma and annealing, while rounder steps appear on the pristine TiO$_2$. This result indicates that the initial presence of the polymer and atomic oxygen pre-treatment affect the subsequent morphology (terrace width and preferential step direction) of the TiO$_2$ surface upon high temperature annealing. Even in the absence of NPs, the TiO$_2$ surface is known to form elongated steps along [001] at high temperature (>900 °C) in order to accommodate a non-stoichiometric composition without destroying the crystalline structure [18]. It is interesting that we do not see these steps on the pristine TiO$_2$ sample after an analogous annealing treatment. We attribute the difference to the distinct roughness and stoichiometry of both supports. An enhanced roughness is expected for the polymer-coated and O$_2$-plasma-treated surface. *Ex situ* AFM investigations of the TiO$_2$(110) surface by Jak [18] also revealed relatively narrow [001] steps on rough TiO$_2$ surfaces upon air exposure.

After annealing at 1060 °C [Fig. 3(e,f)], the majority of the NPs on this sample can be found at TiO$_2$ steps. Since during Pt evaporation all the steps and defect sites on the TiO$_2$ surface were masked by the polymer in this sample, our NPs did not initially form by nucleation at steps (strong binding sites). Instead, significant mass transport (Pt atoms and/or clusters) must have occurred during the O$_2$-plasma and subsequent thermal treatment. In analogy to the case of the Pt NPs evaporated on the pristine TiO$_2$(110) surface, the size histogram from this sample reveals an increase in the average NP height (from ~0.8 nm at 930 °C to 1.3 nm at 1060 °C) [Fig. 4(a)] and an increase in interparticle distance [Fig. 4(b)] with increasing annealing temperature. These effects are accompanied by a decrease in the NP density on the support surface, Table 1(b). An increase in the NP aspect ratio is also observed for this sample with increasing annealing temperature, indicating the decrease in the binding energy of the NPs to the support. As mentioned before, the TiO$_2$ substrate in this sample was exposed to air (*ex situ* polymer coating) before NP deposition, and subsequently O$_2$-plasma treated in UHV (after Pt NP deposition), leading to an oxidized TiO$_2$ surface. However, each subsequent annealing cycle in UHV at high temperature is expected to further reduce the TiO$_2$ surface, strengthening thus the binding of the Pt NPs to TiO$_2$, since oxygen vacancies have been reported to be preferential binding sites for metal NPs [19,41,47–52]. Nevertheless, the increase in the aspect ratio observed (more 3D-like NPs) in spite of the
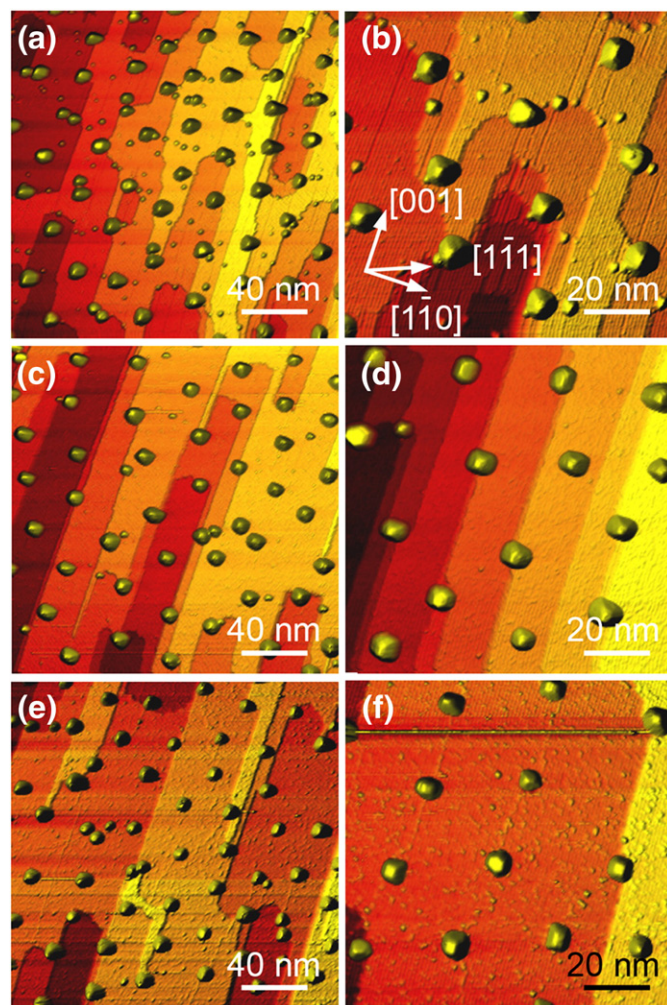
increase in the degree of reduction of the support surface (that should have lead to 2D NPs) can be understood as a size effect, since the interface effect is not as important for the larger NPs formed due to coarsening.

3.3. Micellar Pt NPs/TiO$_2$(110)

Fig. 5 displays STM images from micellar Pt NPs dip-coated on TiO$_2$(110) (S3) after polymer removal and subsequent isochronal annealing in UHV at 1000 °C (a,b), 1060 °C (c,d), and 1060 °C-2nd (e,f) for 10 min. The micellar NPs displayed an enhanced thermal stability as compared to UHV-evaporated Pt clusters, although a bimodal size distribution is also observed on this sample after prolonged annealing at 1060 °C (1060-2nd, 20 min), Figs. 5(e,f) & 6(a). Interestingly, the average interparticle distance and the histogram width did not experience changes upon annealing, Fig. 6(b). Since NPs larger than the original average size were not found on this sample upon annealing, Fig. 6(a), the bimodal size distribution observed here cannot be attributed to coarsening. Possible reasons for such NP size distribution are either Pt desorption after prolonged annealing at 1060 °C, or intrinsic errors in the determination of the NP height for this sample by using as reference either the top or the bottom terraces of the TiO$_2$ substrate for NPs located at the step edges.

Fig. 4. Height (a) and interparticle distance (b) histograms obtained from the STM data of Pt NPs evaporated on polymer-coated TiO$_2$(110) shown in Fig. 3 after an O$_2$-plasma treatment and subsequent annealing at 930 °C (squares), 1030 °C (triangles), and 1060 °C (circles).

Fig. 5. STM images of micellar NPs deposited on TiO$_2$(110) acquired at room temperature after polymer removal by an *in situ* O$_2$-plasma treatment and subsequent isochronal annealing in UHV at 1000 °C (a,b), 1060 °C (c,d), and 1060 °C-2nd (e,f) for 10 min.
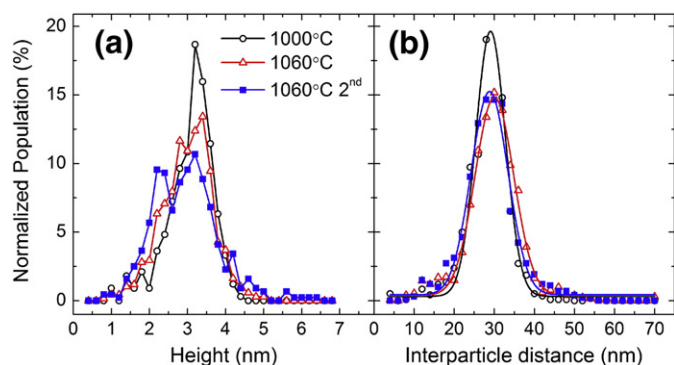
Fig. 6. Average height and interparticle distance histograms obtained from the STM images of micellar Pt NPs shown in Fig. 5 as a function of the annealing temperature. Isochronal annealing (10 min) was carried out in UHV at 1000 °C (open circles), 1060 °C (open triangles), and 1060 °C-2nd (closed squares).

4. Discussion

4.1. STM observations

The data shown above reveal clear changes in the stability of Pt NPs as a function of the preparation method, with micellar Pt NPs being significantly more stable than UHV-evaporated NPs on TiO$_2$(110). In addition, in agreement with previous literature [18–20,41,47–49,52], the coarsening of evaporated Pt NPs appears to be affected by the pretreatment underwent by the support, which leads to drastic changes in its morphology and stoichiometry (surface reduction). For Pt NPs evaporated in UHV, we have observed enhanced coarsening when the NPs were deposited on the polymer pre-coated TiO$_2$ surface (S2), as compared to pristine (sputtered/annealed) TiO$_2$ (S1), indicating weaker NP/support binding in S2. This effect could be partially attributed to the distinct pretreatment that the TiO$_2$ support in S2 underwent prior to the evaporation of Pt NPs, since due to the initial polymer-coating of the TiO$_2$ surface in S2 the Pt NPs were not able to nucleate on stable binding sites such as O-vacancies. In addition, the O$_2$-plasma pre-treatment conducted on S2 after Pt evaporation might have affected the initial stability of the NPs. As will be discussed below, the O$_2$-treatment does not only modify the surface of the TiO$_2$ support, but also that of the Pt NPs, including their oxidation state. For example, Datye et al. [22] explained the enhanced sintering behavior of Pt NPs in air as compared to that under reducing conditions based on the formation of volatile PtO$_x$ species leading to more favorable interparticle mass transport. Although the larger (~3 nm) micellar Pt NPs (S3) were exposed to the same O$_2$-plasma treatment as S2 but did not display any mobility, smaller Pt clusters (S2) are known to experience a more facile oxidation and stronger oxygen binding [39,53], and are therefore expected to be more affected by the oxygen pre-treatment. Nevertheless, the above arguments can only be used to explain the higher coarsening rate of the Pt NPs on the polymer-coated sample well below 930 °C, but not within the temperature regime employed here to monitor coarsening (930 °C–1060 °C). At such elevated temperatures, the Pt NPs and the TiO$_2$ surface are reduced on all three samples.

We consider that the different coarsening trends observed when comparing S1 and S2 after annealing above 930 °C are due to either strong metal support interactions and/or to morphological (rather than chemical) changes induced on TiO$_2$ by the pre-treatment. It is known that Pt NPs are more prone to become encapsulated by TiO$_2$ on a reduced TiO$_2$ substrate [49], and it is possible that the higher extent of TiOx encapsulation on the pristine sample (strongly reduced, S1) as compared to the polymer-coated sample (more oxidized up to 800 °C, S2) is partially responsible for the higher stability against coarsening of S1 [49]. The morphological differences between the TiO$_2$ surfaces in S1 and S2 mentioned above are related to the fact that step edges, known to stabilize NPs [50,54,55], are available on S1 (pristine TiO$_2$)

before Pt deposition, while they only form on the polymer-coated and O$_2$-plasma treated S2 after high temperature annealing.

Jak [18–20] reported a higher growth rate and decoration of steps for Pd NPs evaporated on mildly reduced TiO$_2$(110), while Pd evaporation on strongly reduced TiO$_2$ surfaces gave rise to smaller NPs distributed over the terraces. On the latter surface, the NP mobility was so low that a significant fraction of the NPs were not able to reach the energetically favorable step sites. Analogous findings were reported for Pt [41], Au [51], Cu and Ni on TiO$_2$(110) [54]. We observe a similar behavior in our samples, since some clusters are still seen on the terraces for the Pt/pristine-TiO$_2$ sample at 1060 °C (S1).

Additionally, the work by Goeke and Dayte [32] on the mobility of large Pd clusters deposited on SiO$_2$ and Al$_2$O$_3$ revealed an enhanced rate of sintering for Pd/Al$_2$O$_3$, even though that system is characterized by stronger metal/support interactions than Pd/SiO$_2$. A NP/support combination, where strong metal/support interactions are expected (Pt/pristine-TiO$_2$), does not necessarily lead to more stable NPs. To the contrary, in such cases, the support may assist the mobility of NPs and atoms, leading to more pronounced coarsening patterns at least through the Ostwald-ripening pathway.

Fig. 7 shows the percentage of NPs found on terraces and at step edges for all Pt NP samples. Both evaporated samples show an increase in the percentage of NPs at step edges with increasing annealing temperature, while the micellar sample showed the opposite trend. As was discussed before, the micellar NPs are not mobile, but its presence on the TiO$_2$ surface leads to changes in its morphology (e.g. the presence of narrower terraces or formation of TiO$_2$ nanostripes [34,64]). With increasing annealing temperature, wider terraces and a lower density of step edges are observed in all samples, but the mobile evaporated Pt NPs can still reach those sites, while the immobile micellar NPs won't follow the changes in the support morphology. Despite the lower number of step edges available, the increase in the number of evaporated NPs (S1 and S2) decorating steps after annealing at high temperature is a signature of coarsening. Both coarsening mechanisms could result in NP step-edge decoration. In an Ostwald-ripening model, the step edges would stabilize the NPs and therefore reduce the rate of departing atoms, and eventually favor the growth of NPs at those sites in detriment of those at terraces. On the other hand, in a diffusion-coalescence model, the step edge stabilization would diminish the diffusion of the NPs decorating the steps, and therefore, more mobile NPs (e.g. those at terraces) would eventually coalescence with the stationary (pinned) NPs at the step edges. Therefore, at the elevated temperatures investigated here, coarsening by either Ostwald ripening, diffusion-coalescence, or a combination of both processes, is possible.

Although the shape of the size histograms has been used in the past to differentiate the two fundamental coarsening models (Ostwald-ripening versus diffusion-coalescence), this approach has
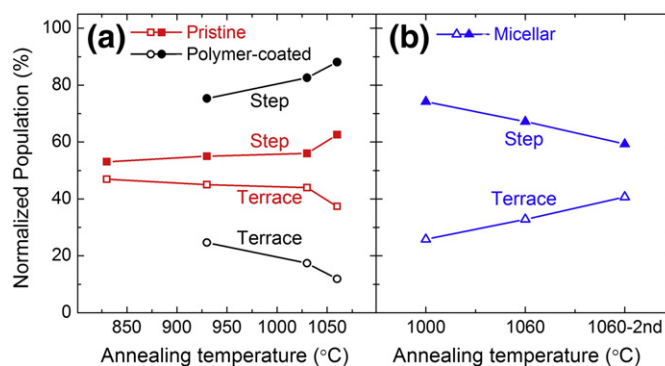
Fig. 7. Thermal evolution of the number of Pt NPs present on the terraces and at step edges for evaporated (a) as well as micellar samples (b).

been questioned by many authors [22,23,32,56]. Howard et al. [56] have studied the mobility of Pd NPs on TiO$_2$(110) using high temperature STM. Although the size histogram obtained after 240 min annealing in UHV at 750 K was skewed toward larger sizes (as expected for diffusion-coalescence), a clear evidence for the diffusion-coalescence mechanism was not observed via STM. Instead, their real time STM measurements at 750 K demonstrated that the Ostwald-ripening pathway was the main coarsening mechanism. Similar experiments on Au/TiO$_2$(110) by Mitchell et al. [23] revealed that both coarsening mechanisms are responsible for the sintering observed, even though their size histograms displayed a bimodal distribution not resembling any of the skewed normal distribution expected for either model.

In addition, although we see fewer and larger NPs in the polymer-coated sample as compared to the pristine sample after annealing, it cannot be necessarily concluded that there is less coarsening for the pristine sample within the range of temperatures shown in Figs. 1 and 3. One must also consider that even though the same amount of Pt was evaporated on both samples, the initial sample pre-treatment might affect the nucleation and growth dynamics of the NPs and therefore, their initial size distribution. In particular, the presence of the polymer on the TiO$_2$ surface of S2 could have led to an initially larger average size distribution which could have propagated after annealing, leading to the size differences observed at 930 °C between S1 and S2 (see Table 1). In addition to the possible distinct nucleation of Pt atoms and Pt NP growth on reduced TiO$_2$ (pristine sample, S1) as compared to polymer-coated TiO$_2$, S2 coarsening might also have occurred during the subsequent O$_2$-plasma treatment underwent by S2 due to the formation of volatile PtO$_x$ species. Because of the enhanced roughness of the TiO$_2$ support after the latter treatment, the NPs could not be resolved, and the coarsening behavior of all samples is only compared after annealing at high temperature (≥930 °C), when all TiO$_2$ surfaces are strongly reduced and no PtO$_x$ is available. Although theoretically ideal, it is not experimentally possible to obtain identical initial NP size distributions and NP

densities on the TiO$_2$ surface after the different surface functionalizations described here. To overcome this issue, our simulation approach is useful, since it takes into account implicitly the former effects. In particular, the coarsening behavior of samples with different initial size distributions and NP densities can be contrasted by comparing the fitting parameters E_{tot} and K_S. For instance, large E_{tot} and small K_S values are indicative of a higher resistance toward coarsening.

To the best of our knowledge, real-time (live) STM or TEM measurements of NP coarsening at the elevated temperatures employed here have not been reported due to instrumentation limitations. The above discussion demonstrates the need of having a more reliable method to understand the main coarsening mechanism underlying our experimental observations and to obtain coarsening rates. The dominant coarsening mechanism is determined here based on simulations of the size histograms following two different sintering models.

4.2. Simulation of coarsening mechanism

4.2.1. Ostwald ripening

Fig. 8 displays simulations of the evolution of the NP height for Pt NPs evaporated on (a) pristine TiO$_2$ and (b) polymer-coated TiO$_2$ following the Ostwald-ripening model described in the theoretical methods section. Each simulation uses an experimental size distribution as starting point and calculates the evolution of such distribution during a given annealing treatment. Since the NPs are assumed to be hemispherical, the values of R in Eq. (1) are identical to the NP height (shown in the plots). Each experimental thermal treatment consists of three segments: (i) a ramp to the target annealing temperature (1030 °C or 1060 °C) with a rate of 1.5 °C/s, (ii) annealing at a constant target temperature for 10 min, and (iii) a second ramp to decrease the sample temperature to room temperature with the same rate as in (i). Each graph in Fig. 8 shows the initial experimental histogram (full curve with hatched-pattern filled area) and the subsequent experimental NP size distribution after the thermal treatment
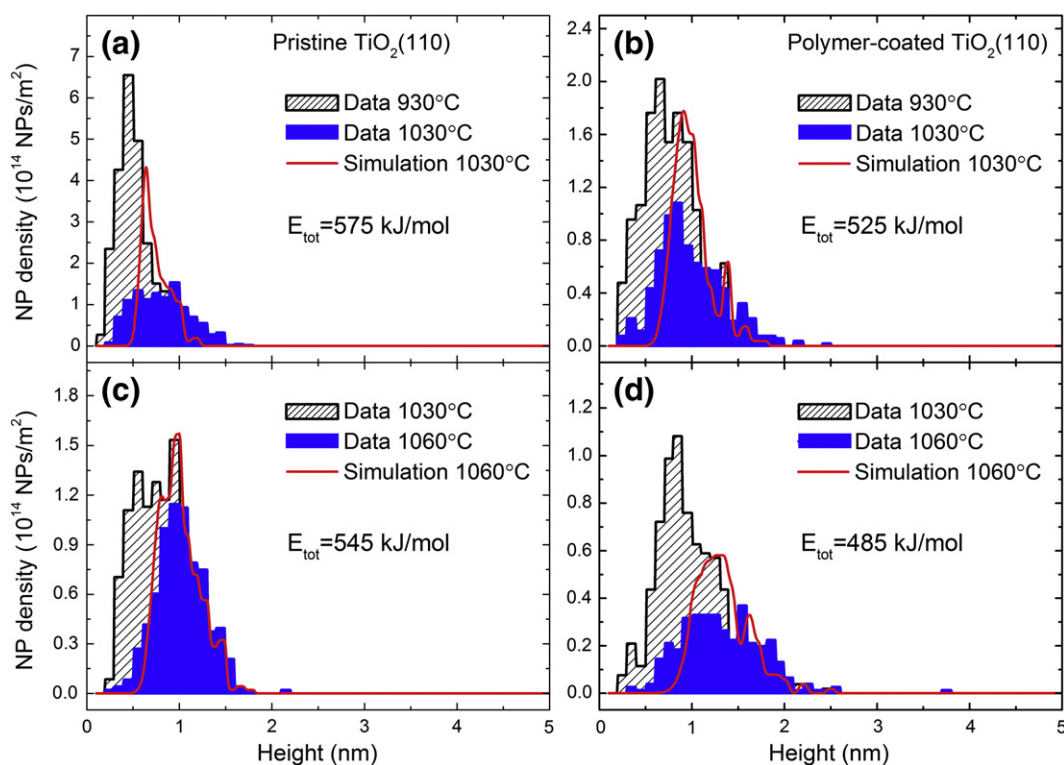
Fig. 8. Best fits obtained from Ostwald-ripening simulations of the pristine (a,c) and polymer-coated (b,d) Pt/TiO$_2$(110) samples. The hatched and solid filled areas are the initial and the final experimental size distributions, respectively. The solid line displays the simulated final size distribution obtained after annealing treatments in UHV at 1030 °C (a,b) and 1060 °C (c,d).

Table 2
Total energy barrier (E_{tot}), support effect (K_S), and diffusion coefficient (D_c) obtained from the best fit of the Ostwald-ripening and diffusion-coalescence models to our experimental NP size histograms. The experimental data correspond to UHV evaporated Pt NPs deposited on pristine and polymer-coated TiO$_2$(110). The estimated errors are given within parenthesis.

	Annealing temperature (°C)	Pristine TiO$_2$ (S1)	Polymer-coated TiO$_2$ (S2)
Ostwald-ripening	1030	575 (10)	525 (15)
E_{tot} (kJ/mol)	1060	545 (20)	485 (10)
Diffusion-coalescence	1030	$1.3 \times (1.3^{\pm 1})$	$4 \times (1.5^{\pm 1})$
K_S (10^{-3})		5.5	5.8
D_c ($\times 10^{-26}$ m^2/s)	1060	$1.7 \times (1.7^{\pm 1})$	$13 \times (1.3^{\pm 1})$
		4.6	18.0

(full curve with solid filled area), together with the results from the simulation at 1030 °C (a,b) and 1060 °C (c,d) (red solid curves).

The only fitting parameter was the total energy barrier of the system E_{tot}, varied within the range of 100 to 600 kJ/mol. The best fit was selected as such having the same NP surface density (number of NPs/surface area) than the experimental data after the annealing cycle. Although the peak positions of the simulated histograms are similar to the experimental data, a common feature in all simulations is their narrower size distribution as compared to the experimental results.

The best E_{tot} values extracted from our simulations are shown in Table 2. The error bars were defined as the deviation in E_{tot} needed to obtain a 10% change in the NP surface density with respect to the experimental value. The total energy barrier obtained for the Pt NPs evaporated on the polymer-coated sample was found to be ~50 kJ/mol lower than that of the pristine sample, demonstrating a higher coarsening rate. Another interesting result is the ~30–40 kJ/mol decrease in E_{tot} for these samples after the second annealing cycle (1060 °C). This result is in agreement with the increase in the NP aspect ratio described in the previous section with increasing annealing temperature, leading to a decreased NP/support interaction

(dewetting) and to a weaker support effect for the larger NPs formed at the highest temperatures.

Considering the heat of sublimation of platinum (563 kJ/mol) [57] and the adsorption energy of Pt monomers on TiO$_2$(110) [58,59] (~3.5 eV on O-vacancy sites and ~2.1 eV on hollow sites with an average value of ~2.8 eV or 272 kJ/mol) and the diffusion barrier of Pt on TiO$_2$(110) [58,59] (~2.1 eV for the [100] direction and ~0.9 eV for [110], with an average value of ~1.5 eV or 147 kJ/mol) we could estimate E_{tot} from:

$$E_{tot} = \Delta H_{sub} + H_m^S - E_{ad}^S, \qquad (8)$$

where ΔH_{sub} is the bulk heat of sublimation and H_m^S and E_{ad}^S are the diffusion barrier and adsorption energy of metal atoms on the support, respectively. According to Eq. (8), a typical value for the total energy barrier of Pt on the TiO$_2$ surface is 438 kJ/mol, and in comparison, all of the E_{tot} values obtained from our simulations are larger. It should be however noted that the overall agreement between simulated and experimental data is not good for this model.

4.2.2. Diffusion-coalescence

The same thermal treatment described in the previous section was used for the diffusion-coalescence simulations. Fig. 9 displays the NP density versus NP height. The results of the best fits (solid curves), together with the initial (full curves with filled hatched area) and final (full curves with solid filled area) experimental histograms, are also shown in Fig. 9. The following constant parameters were used in the simulations: $D = 10^{-7}$ m^2/s for Pt monomers on Pt(111) [57,60] and $\rho_0 = 1.5 \times 10^{19}$ 1/m^2. In this case, the calculations were done using the NP volume distribution, since the volume is the independent variable in Eq. (3) (see Suppl. Fig. S4). The volumes were obtained from STM measurements of the NP height assuming a hemispherical NP shape. In Fig. 9, the simulation results were rescaled from NP volume to NP height to be consistent with the STM measurements as well as to allow the direct comparison with the results of the
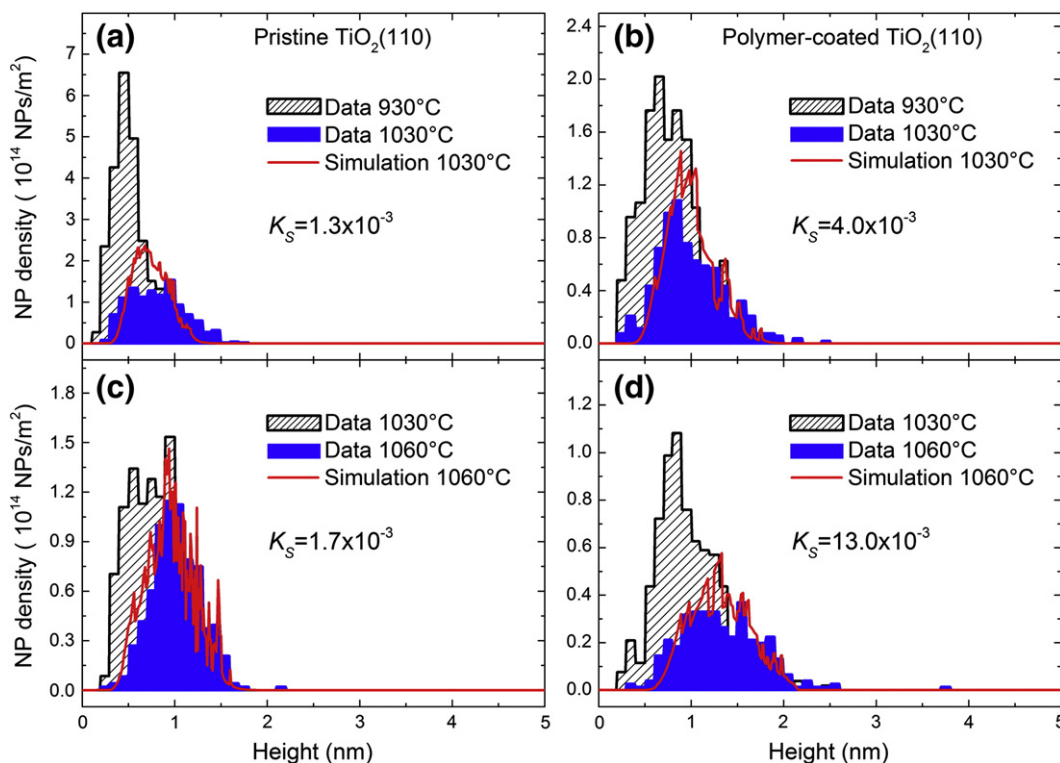
Fig. 9. Best fits obtained from a diffusion-coalescence simulation for pristine (a,c) and polymer-coated (b,d) Pt/TiO$_2$(110) samples. The hatched and solid filled areas are the initial and the final experimental size distributions, respectively. The solid line displays the simulated final size distribution obtained after annealing treatments in UHV at 1030 °C (a,b) and 1060 °C (c,d).

Ostwald ripening simulations. The only fit parameter used in the simulation is K_S. The simulation results are in good agreement with the experimental data for both samples, especially after the second annealing treatment. The K_S values obtained for the pristine and polymer-coated samples are shown in Table 2. Since the parameter K_S entails support effects (NP pinning and step-edge stabilization), which normally lead to decreased diffusion rates, it is expected to be smaller than 1, as obtained in our simulations ($\sim 10^{-3}$, Table 2). Despite the initial larger average NPs size (at 930 °C), and similar to our findings based on the Ostwald-ripening model, a more pronounced coarsening was evidenced for the polymer-coated sample as compared to the pristine sample. In addition, a higher diffusion rate was also observed during the second annealing cycle (1060 °C).

In order to conclude which coarsening pathway better describes our experimental data, a fit quality parameter (Q) must be defined. Efron's pseudo-R^2 parameters ($R^2_{pseudo} = Q$) were used to evaluate the goodness of the fit of the simulated histograms to the experimental data [61]. However, due to statistical fluctuations in both, simulated and experimental histograms, data smoothing (spline fit) was conducted before the comparison. A quality factor $Q = 1$ represents a perfect agreement between simulated and experimental data, and lower values a larger mismatch. The details of the mathematical procedure used to calculate Q are provided in the suppl. documents and Suppl. Fig. 5.

The resulting fit quality factors, Q, are given in Table 3. For the polymer pre-coated sample (S2), the quality of the simulation is considerably better for the diffusion-coalescence model as compared to the Ostwald ripening model during both thermal treatments. This is mainly due to the fact that size distributions narrower than those in the experimental data result from the Ostwald ripening simulations. Therefore, we conclude that the diffusion-coalescence pathway is the dominant coarsening mechanism underwent by the NPs in this sample. A similar conclusion can be drawn for the first thermal treatment (1030 °C histogram) of the NPs supported on the pristine TiO$_2$(110) surface (S1). However, for the second thermal treatment (1060 °C histogram), a relatively good agreement between the simulation and experimental data was observed for both models. However, the total energy barrier obtained from the Ostwald ripening model ($E_{tot} = 545$ kJ/mol) is excessively large as compared to the expected theoretical value ($E_{tot} \approx 438$ kJ/mol). Therefore, the Ostwald ripening pathway can be ruled out. The fitting parameters obtained following the diffusion coalescence model (K_S) are reasonable for all samples and similar to those obtained by Jak et al. [19] for the Pd/TiO$_2$ system. Accordingly, the diffusion-coalescence pathway is assigned as the dominant sintering mechanism for all of our PVD-grown Pt NPs.

Considering the average NP height (Table 1), K_S (Table 2), and the adatom formation energy barrier (Suppl. Fig. S3), the NP diffusion coefficient [D_c in Eq. (5)] was obtained for S1 and S2 for both annealing treatments and reported in Table 2. The smallest D_c value was found for the pristine sample (S1) during the second thermal treatment (1030 °C to 1060 °C), indicating reduced NP mobility. Interestingly, the values of the coarsening parameters obtained from the simulations after annealing at 1030 °C [support effect (K_S)] indicate the higher stability of our Pt NPs as compared to model hemispherical NPs. Nevertheless, a decrease in their stability, approaching the

theoretical values, was observed with increasing annealing temperature. The latter effect correlates with the increase in the NP aspect ratio (height to radius) and can be understood in terms of substrate de-wetting leading to NP de-stabilization. Carrey et al. [62] previously showed that small NPs trapped by surface defects could be released after sintering phenomena lead to the formation of larger NPs.

In order to directly observe and determine the coarsening mechanism, in situ real-time microscopic data at temperatures exceeding 900 °C will be needed. However, such studies cannot be implemented experimentally to date due to instrumentation limitations (large drift), justifying thus the present approach.

5. Conclusions

The thermal stability, mobility, and coarsening of Pt NPs supported on TiO$_2$(110) was investigated by combining STM measurements with simulations of cluster size. The effect of the substrate pre-treatment, roughness, and degree of reduction on the coarsening of metallic NPs deposited on oxide supports was discussed. Evaporated Pt NPs show a stronger binding to the strongly reduced pristine TiO$_2$(110) as compared polymer-coated and O$_2$-plasma treated TiO$_2$(110). Furthermore, the support-induced stability appears to be stronger for the smaller NPs.

Modifications to the traditional mathematical description of the diffusion-coalescence coarsening model were implemented to better describe the temperature dependence of the diffusion constant as well as to incorporate physically meaningful energetics for adatom formation in NPs. In addition, more efficient computational methods to simulate coarsening phenomena following the Ostwald ripening and diffusion-coalescence models were developed. The efficiency of such simulation methods is essential in order to be able to follow industrially relevant sintering processes that are likely to occur over extended periods of time. Our mathematical description facilitates the comparison of coarsening phenomena occurring on NP samples supported on distinct substrates. Our simulations revealed that the diffusion-coalescence model provides a considerably better description of our experimental data for evaporated NPs (S1, S2) as compared to the Ostwald-ripening model. On the other hand, no changes in the NP size distribution were observed for the larger micellar Pt NPs after identical thermal treatments. The advantages of the stabilization of NPs within the size range of our micellar Pt NPs (~3 nm at ~1060 °C) should be recognized, since such sizes have been reported to be the active for certain catalysis applications [63]. Thus, micellar-based NP fabrication methods may be considered excellent candidates for the production of rationally-engineered active and durable nanocatalysts.

Appendix A. Supplementary data

Supplementary data to this article can be found online at doi:10.1016/j.susc.2012.01.022.

Table 3
Simulation quality factors (Q) for pristine (S1) and polymer pre-coated (S2) samples obtained for the Ostwald-ripening and diffusion-coalescence coarsening models.

Sample	Temperature (°C)	Q diffusion-coalescence	Q Ostwald ripening
Pristine (S1)	1030	0.57	− 0.33
	1060	0.92	0.90
Polymer pre-coated (S2)	1030	0.86	0.18
	1060	0.96	0.31

References

[1] C.R. Henry, Surf. Sci. Rep. 31 (1998) 231.
[2] B. Roldan Cuenya, Thin Solid Films 518 (2010) 3127.
[3] C.T. Campbell, Surf. Sci. Rep. 27 (1997) 1.
[4] A.K. Santra, D.W. Goodman, J. Phys. Condens. Matter 14 (2002) R31.

[5] J.M. Thomas, W.J. Thomas (Eds.), Principles and Practice of Heterogeneous Catalysis, VCH, Weinheim, 1997.
[6] M. Haruta, Catal. Today 36 (1997) 153.
[7] L.M. Petkovica, D.M. Ginosara, H.W. Rollinsa, K.C. Burcha, C. Deianab, H.S. Silvab, M.F. Sardellab, D. Granadosb, Int. J. Hydrogen Energy 34 (2009) 4057.
[8] V.R. Choudhary, K.C. Mondal, A.S. Mamman, J. Catal. 233 (2005) 36.
[9] D.M. Ginosar, H.W. Rollins, L.M. Petkovic, K.C. Burch, M.J. Rush1, Int. J. Hydrogen Energy 34 (2009) 4065.
[10] S.N. Rashkeev, D.M. Ginosar, L.M. Petkovic, H.H. Farrell, Catal. Today 139 (2009) 291.
[11] L.M. Petkovic, D.M. Ginosar, H.W. Rollins, K.C. Burch, P.J. Pinhero, H.H. Farrell, Appl. Catal., A 338 (2008) 27.
[12] M. Ni, M.K.H. Leung, D.Y.C. Leung, K. Sumathy, Renewable Sustainable Energy Rev. 11 (2007) 401.
[13] A.L. Linsebigler, G. Lu, J.T. Yates, Chem. Rev. 95 (1995) 735.
[14] S.C. Parker, C.T. Campbell, Top. Catal. 44 (2007) 3.
[15] C.T. Campbell, S.C. Parker, D.E. Starr, Science 317 (2002) 44.
[16] S.C. Parker, C.T. Campbell, Phys. Rev. B 75 (2007) 035430.
[17] P.A. Thiel, M. Shen, D.-J. Liu, J.W. Evans, J. Phys. Chem. C 113 (2009) 5047.
[18] Jak, M. J. J., PhD thesis, Leiden University, 2000.
[19] M.J.J. Jak, C. Konstapel, A. Van Kreuningen, J. Chrost, J. Verhoeven, J.W.M. Frenken, Surf. Sci. 474 (2001) 28.
[20] M.J.J. Jak, C. Konstapel, A. van Kreuningen, J. Verhoeven, J.W.M. Frenken, Surf. Sci. 457 (2000) 295.
[21] A. El-Azab, S. Gan, Y. Liang, Surf. Sci. 506 (2002) 93.
[22] A.K. Datye, X. Qing, K.C. Kharas, J.M. McCarty, Catal. Today 111 (2006) 59.
[23] C.E.J. Mitchell, A. Howard, M. Carney, R.G. Egdell, Surf. Sci. 490 (2001) 196.
[24] P. Stone, S. Poulston, R.A. Bennett, M. Bowker, Chem. Commun. (1998) 1369.
[25] M.v Smoluchowski, Phys. Z. 17 (1916) 585.
[26] M.v Smoluchowski, Z. Phys. Chem. 92 (1917) 129.
[27] P. Wynblatt, N.A. Gjostein, Prog. Solid State Chem. 9 (1975) 21.
[28] P. Wynblatt, N.A. Gjostein, Acta Metall. 24 (1976).
[29] D. Kandel, Phys. Rev. Lett. 79 (1997) 4238.
[30] C.G. Granqvist, R.A. Duhrman, J. Catal. 42 (1976) 477.
[31] J.G. McCarty, G. Malukhin, D.M. Poojary, A.K. Datye, Q. Xu, J. Phys. Chem. B 109 (2005) 2387.
[32] R.S. Goeke, A. Datye, Top. Catal. 46 (2007) 3.
[33] B. Roldan Cuenya, S.H. Baeck, T.F. Jaramillo, E.W. McFarland, J. Am. Chem. Soc. 125 (2003) 12928.
[34] A. Naitabdi, F. Behafarid, B. Roldan Cuenya, Appl. Phys. Lett. 94 (2009) 083102.
[35] U. Diebold, Surf. Sci. Rep. 48 (2003) 53.
[36] A. Naitabdi, L.K. Ono, F. Behafarid, B. Roldan Cuenya, J. Phys. Chem. C 113 (2009) 1433.
[37] L.K. Ono, B. Roldan Cuenya, J. Phys. Chem. C 112 (2008) 4676.
[38] A. Naitabdi, B. Roldan Cuenya, Appl. Phys. Lett. 91 (2007) 113110.
[39] L.K. Ono, B. Yuan, H. Heinrich, B. Roldan Cuenya, J. Phys. Chem. C 114 (2010) 22119.
[40] C. Xu, X. Lai, D.W. Goodman, Faraday Discuss. 105 (1996) 247.
[41] J.B. Park, S.F. Conner, D.A. Chen, J. Phys. Chem. C 112 (2008) 5490.
[42] B. Roldan Cuenya, J.R. Croy, S. Mostafa, F. Behafarid, L. Li, Z. Zhang, J.C. Yang, Q. Wang, A.I. Frenkel, J. Am. Chem. Soc. 132 (2010) 8747.
[43] O. Dulub, W. Hebenstreit, U. Diebold, Phys. Rev. Lett. 84 (2000) 3646.
[44] J. Szoko, A. Berko, Vacuum 71 (2003) 193.
[45] L.R. Houk, S.R. Challa, B. Grayson, P. Fanson, A.K. Datye, Langmuir 25 (2009) 11225.
[46] J. Yang, W. Hu, S. Chen, J. Tang, J. Phys. Chem. C 113 (2009) 21501.
[47] F. Yang, M.S. Chen, D.W. Goodman, J. Phys. Chem. C 113 (2009) 254.
[48] D.N. Belton, Y.-M. Sun, J.M. White, J. Phys. Chem. 88 (1984) 1690.
[49] S.J. Tauster, Acc. Chem. Res. 20 (1987) 389.
[50] X. Lai, T.P.S. Clair, M. Valden, D.W. Goodman, Prog. Surf. Sci. 59 (1998) 25.
[51] E. Wahlstrom, N. Lopez, R. Schaub, P. Thostrup, A. Rønnau, C. Africh, E. Lægsgaard, J.K. Norskov, F. Besenbacher, Phys. Rev. Lett. 90 (2003) 026101.
[52] D.C. Schlober, K. Morgenstern, L.K. Verheij, G. Rosenfeld, F. Besenbacher, G. Comsa, Surf. Sci. 465 (2000) 19.
[53] S. Mostafa, F. Behafarid, J.R. Croy, L.K. Ono, L. Li, J.C. Yang, A.I. Frenkel, B. Roldan Cuenya, J. Am. Chem. Soc. 132 (2010) 15714.
[54] J. Zhou, Y.C. Kang, D.A. Chen, Surf. Sci. 537 (2003) 429.
[55] C. Xu, X. Lai, G.W. Zajac, D.W. Goodman, Phys. Rev. B 56 (13) (1997) 464.
[56] A. Howard, C.E.J. Mitchell, R.G. Egdell, Surf. Sci. 515 (2002) 504.
[57] N. Panagiotides, N.I. Papanicolaou, Int. J. Quantum Chem. 110 (2009) 202.
[58] H. Iddir, S. Öğüt, N.D. Browning, M.M. Disko, Phys. Rev. B 72 (2005) 081407.
[59] H. Iddir, V. Skavysh, S. Öğüt, N.D. Browning, M.M. Disko, Phys. Rev. B 73 (2006) 041403.
[60] M. Bott, M. Hohage, M. Morgenstern, T. Michely, G. Comsa, Phys. Rev. Lett. 76 (1996) 1304.
[61] J.W. Hardin, J.M. Hilbe, J. Hilbe, Generalized Linear Models and Extensions, 2nd edition Stata Press, 2007.
[62] J. Carrey, J.L. Maurice, F. Petroff, A. Vaurès, Phys. Rev. Lett. 86 (2001) 4600.
[63] M. Valden, Science 281 (1998) 1647.
[64] F. Behafarid, B. Roldan Cuenya, J. Phys. Chem. Lett. 3 (2012) 608.